

See discussions, stats, and author profiles for this publication at: <https://www.researchgate.net/publication/268331980>

# Zn Ion Post-Implantation-Driven Synthesis of CuZn Alloy Nanoparticles in Cu-Preimplanted Silica and Their Thermal Evolution

ARTICLE in ACS APPLIED MATERIALS & INTERFACES · DECEMBER 2014

Impact Factor: 6.72

---

READS

29

## 4 AUTHORS, INCLUDING:



Guangyi Jia

Tianjin University

14 PUBLICATIONS 21 CITATIONS

SEE PROFILE



Xiaoyu mu

Tianjin University

7 PUBLICATIONS 10 CITATIONS

SEE PROFILE

# Zn Ion Post-Implantation-Driven Synthesis of CuZn Alloy Nanoparticles in Cu-Preimplanted Silica and Their Thermal Evolution

Guangyi Jia,<sup>†</sup> Rong Xu,<sup>†</sup> Xiaoyu Mu,<sup>†</sup> and Changlong Liu<sup>\*,†,‡,§</sup>

<sup>†</sup>School of Science, Tianjin University, Tianjin 300072, P. R. China

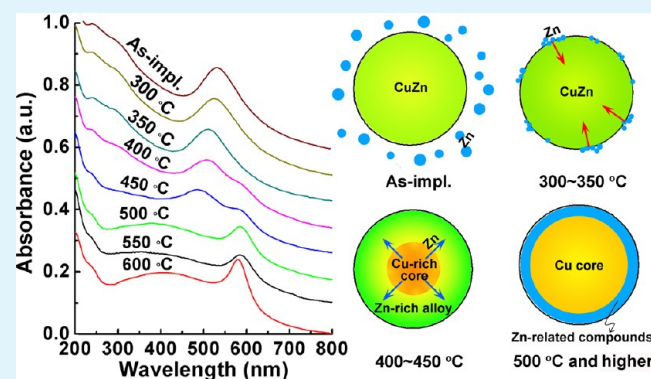
<sup>‡</sup>Tianjin Key Laboratory of Low Dimensional Materials Physics and Preparation Technology, Institute of Advanced Materials Physics Faculty of Science, Tianjin 300072, P. R. China

<sup>§</sup>Key Laboratory of Beam Technology and Material Modification of the Ministry of Education, Beijing Normal University, Beijing 100875, P. R. China

## S Supporting Information

**ABSTRACT:** Cu nanoparticles (NPs) were fabricated in silica by 45 keV Cu ion implantation at a fluence of  $1.0 \times 10^{17} \text{ cm}^{-2}$  and were then subjected to implantation of 50 keV Zn ions at fluences of  $1.0 \times 10^{16}$ ,  $5.0 \times 10^{16}$ , and  $10.0 \times 10^{16} \text{ cm}^{-2}$ , respectively. Our results clearly show that post Zn ion implantation could significantly modify structures and components of the preformed Cu NPs and thus the corresponding surface plasmon resonance (SPR) absorption can be modulated in a wide range. In particular, CuZn alloy NPs with unique SPR absorption were synthesized in Cu-implanted silica followed by Zn ion implantation at a fluence of  $5.0 \times 10^{16} \text{ cm}^{-2}$ . During subsequent annealing, two distinguished processes concerning CuZn alloy NPs (i.e., realloying and dealloying) were found that directly result from thermally driven diffusion of Zn atoms. Moreover, owing to Zn diffusion, lots of core-shell nanostructures consisting of Zn-related compound shells around Cu cores were observed after annealing at 500 °C and higher. The underlying mechanism concerning the formation and decomposition of CuZn alloy NPs is discussed and presented.

**KEYWORDS:** sequential ion implantation, CuZn alloy nanoparticles, thermal diffusion, optical properties, core-shell nanostructure



## 1. INTRODUCTION

Metal nanoparticles (NPs) embedded in the insulating matrixes have attracted increasing interest in recent decades because of their peculiar optical, magnetic, and catalytic properties with prospective applications in various fields.<sup>1</sup> For example, owing to the impressive linear and nonlinear optical properties, glass-based nanocomposites containing noble-metal (e.g., Au, Ag, and Cu) NPs are considered to be excellent candidates for the fabrication of ultrafast optical switches, optical sensors, and antibacterial materials.<sup>2–5</sup> Recently, the formation of bimetallic NPs with particular arrangements, such as core-shell or alloy structures, has become the subject of much research because by controlling the particle composition the properties of the nanocomposites might be further tuned over a relatively wider range.<sup>6</sup> Among the possible methods to synthesize monometallic or bimetallic NPs in dielectrics, ion implantation has proven to be a nonequilibrium technique substantially applicable to any combination of ion species and target materials with well-controlled concentration and spatial position.<sup>7,8</sup> In particular, the sequential ion implantation of two different ion species of metals with higher miscibility is possible to form binary alloy NPs if the implantation

parameters are prudently chosen to maximize the overlap between the concentration profiles of the two implants. Until now, a variety of binary alloy NPs in glass have been fabricated by means of sequential ion implantation, such as Au–Ag, Au–Cu, and Cu–Ni, and others,<sup>9–12</sup> which exhibit a quite different surface plasmon resonance (SPR) response from those related to the monometallic NPs of the constituent species. Although the sequential ion implantation adds a further degree of freedom to the engineering of new material properties, it is difficult to determine in advance whether the desired alloy NPs can be formed in the substrate without any post treatment because many factors can exert a strong influence upon the concentration profiles of the implants along with the nucleation and growth of NPs, such as the implantation sequence, surface-sputtering effect, ion-beam heating, radiation-induced defects, chemical interaction of the implanted elements with the host matrix, and so forth.<sup>12,13</sup>

**Received:** September 14, 2013

**Accepted:** November 27, 2013

**Published:** November 27, 2013

As a category of age-old materials, CuZn alloys have been well-known and used for coins and ornamental purposes since the beginning of metallurgy.<sup>14,15</sup> Recent studies have shown that CuZn alloys are also potentially of interest for industrial water treatment and antifouling research because of their corrosion-resistant ability and catalytic property.<sup>16–19</sup> On the basis of the high miscibility (maximum solid solubility of about 38.4 atom %<sup>20</sup>) and negative mixing heat (about  $-1800$  cal/mol<sup>21</sup>) of Cu and Zn metals as well as their high interdiffusion coefficients,<sup>22</sup> one can expect that CuZn alloy NPs could be fabricated in host matrixes via the dual implantation of two ion species. Actually, in our previous work,<sup>23</sup> when Cu ions at normal incidence and Zn ions at oblique incidence with  $45^\circ$  from the sample surface were sequentially implanted into amorphous SiO<sub>2</sub> (a-SiO<sub>2</sub>) at the same energy (45 keV) and fluence ( $1.0 \times 10^{17}$  cm<sup>-2</sup>), CuZn alloy NPs were substantially demonstrated to be formed in the substrate after 500 °C annealing under nitrogen ambient, which exhibited a strong SPR absorption peak at about 515 nm. However, until now, lots of aspects concerning the CuZn alloy NPs, such as the formation conditions, thermal stability, component-dependent optical properties, underlying mechanism, and so forth, are still unclear.

In this work, Cu NPs were fabricated into a-SiO<sub>2</sub> slices by implantation of 45 keV Cu ions at a fluence of  $1.0 \times 10^{17}$  cm<sup>-2</sup> and were then subjected to 50 keV Zn ion implantation at different fluences. The structures, optical properties, and thermal stability of the fabricated NPs were investigated in detail. Our results clearly show that CuZn alloy NPs in silica via Cu and Zn ion sequential implantation could be formed at an appropriate fluence without any post thermal treatments. Moreover, two distinguished processes concerning CuZn alloy NPs under annealing (i.e., realloying and dealloying) were revealed, which have been demonstrated to be closely related to thermal-driven diffusion of Zn atoms. In addition, the formation of core-shell structures were also revealed during subsequent annealing, which provides an effective method to tailor the optical absorption property.

## 2. EXPERIMENTAL SECTION

On a metal vapor vacuum arc (MEVVA) implanter, optical-grade a-SiO<sub>2</sub> slices of 1.0 mm in thickness were implanted with 45 keV Cu ions at a fluence of  $1.0 \times 10^{17}$  cm<sup>-2</sup>, and some of the Cu ion implanted slices were then implanted with 50 keV Zn ions to fluences of  $1.0 \times 10^{16}$ ,  $5.0 \times 10^{16}$ , and  $10.0 \times 10^{16}$  cm<sup>-2</sup>, respectively. For convenience, the Cu ion implanted specimens were labeled as the Cu sample, and the Cu first followed by Zn ion implanted samples were named as Cu + 1.0 Zn, Cu + 5.0 Zn, and Cu + 10 Zn according to the adopted Zn ion fluence, respectively. During implantation, the incident ion beam was set to be perpendicular to the sample surface, and the flux density was kept at  $4 \mu\text{A}/\text{cm}^2$  or lower to prevent sample overheating. After implantation, the SiO<sub>2</sub> slices were cut into small pieces and were furnace-annealed at different temperatures for 1 h in flowing nitrogen ambient.

The concentration profiles of implants in the prepared samples were probed by Rutherford backscattering spectrometry (RBS) with a 2.02 MeV He ion beam at a scattering angle of  $165^\circ$ . The optical absorption responses related to the formation of monometallic or bimetallic NPs were investigated by using a UV-3600 double-beam spectrophotometer in a wavelength range from 200 to 800 nm. The scanning interval and the bandwidth were set as 0.5 and 2.0 nm, respectively. Grazing incidence X-ray diffraction (GIXRD) measurements were made on a Philips X'pert pro diffractometer using Cu K $\alpha$  line ( $\sim 0.154$  nm) at an incident angle of  $0.3^\circ$  with a scanning speed of  $1^\circ/\text{min}$  to characterize the structure of the NPs as well as their thermal evolution. Moreover,

cross-sectional transmission electron microscope (XTEM) observations were conducted on a Tecnai G2 F20 S-Twin microscope operating at an acceleration voltage of 200 kV. Bright-field imaging and selected-area electron diffraction (SAED) techniques were used to evaluate the shape, size, and spatial distribution of the formed NPs along with their structures. Additionally, energy-dispersive X-ray spectroscopy (EDXS) was also employed to analyze the elemental composition of both NPs and their surrounding media.

## 3. RESULTS AND DISCUSSION

It has been well-demonstrated that the structures, sizes, and spatial distributions of NPs synthesized via ion implantation depend strongly on the profiles of the implants.<sup>24</sup> Therefore, it is crucial to determine in advance the distributions of the implants experimentally and theoretically. In fact, owing to the large sputtering erosion of the surface for heavy ion implantation at low energy, the fluence-dependent depth distribution function of implants in a substrate can be expressed as<sup>25</sup>

$$G(z) = \frac{N}{2Y} \left( \operatorname{erf} \left( \frac{z - R_p + \Phi Y/N}{\sqrt{2} \cdot \Delta R_p} \right) - \operatorname{erf} \left( \frac{z - R_p}{\sqrt{2} \cdot \Delta R_p} \right) \right) \quad (1)$$

where  $z$  is the depth coordinate with respect to the instantaneous surface,  $N$  is the atomic density of the substrate,  $Y$  is the sputtering yield,  $\Phi$  is the ion fluence,  $R_p$  is the projected range of ions,  $\Delta R_p$  is the range straggling related to  $R_p$ , and erf is the error function. Considering the thickness  $d = \Phi \times Y/N$  of the sputtered surface layer induced by post Zn ion implantation in our case, the concentration profiles of Cu and Zn atoms in the implanted SiO<sub>2</sub> could be calculated using eq 1, where  $R_p$ ,  $\Delta R_p$ , and  $Y$  could be obtained through SRIM 2010 simulations.<sup>26</sup> The simulated results are shown in Figure 1.

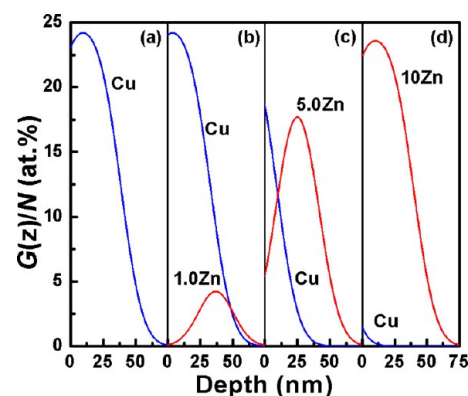


**Figure 1.** Simulated concentration profiles of Cu and/or Zn atoms in the (a) Cu, (b) Cu + 1.0 Zn, (c) Cu + 5.0 Zn, and (d) Cu + 10 Zn samples using eq 1.

One can clearly see that under post Zn ion implantation the profile of preimplanted Cu atoms could be largely modified, which depends strongly on the Zn ion fluence. At the low fluence of  $1.0 \times 10^{16}$  cm<sup>-2</sup>, the sputtering loss of Cu is low, and the profiles of Cu and Zn atoms are nearly overlapping. At the intermediate fluence of  $5.0 \times 10^{16}$  cm<sup>-2</sup>, the sputtering effect induces significant loss of Cu together with a profile shift toward the surface. Nevertheless, one can see that the profiles of Cu and Zn atoms overlap in a wide range and that their contents are comparable. However, as Zn ion fluence increases up to  $1.0 \times 10^{17}$  cm<sup>-2</sup>, it is found that most of the preimplanted

Cu atoms have been removed and Zn atoms with high concentration are distributed in the substrate.

The loss of Cu and its profile shift were confirmed by RBS measurements, as presented in Figure 2. It can be seen from the

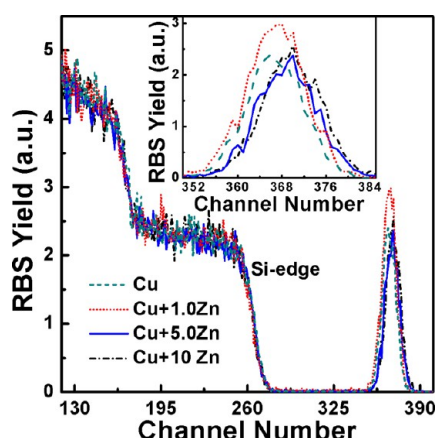


**Figure 2.** RBS spectra of the Cu, Cu + 1.0 Zn, Cu + 5.0 Zn, and Cu + 10 Zn samples. The inset shows the magnified profiles of the implants for clarity.

figure that in the Cu sample the Cu profile is mainly distributed in channel range of 350–380. Post Zn ion implantation at a fluence of  $1.0 \times 10^{16} \text{ cm}^{-2}$  leads only to an intensity increase of the profile without a position change, indicating that the sputtering loss of Cu is negligible. The intensity increase is directly related to the introduction of Zn atoms in the same region because the atomic masses of Zn and Cu are very close. The result is quite agreeable with that calculated using eq 1. As for the Cu + 5.0 Zn sample, the profile shifts to the high-channel side (i.e., surface side). However, its intensity changes less as compared with that in the Cu sample. The result reveals that almost half of Cu has been removed because of the sputtering effect. As Zn ions were post implanted at the fluence of  $1.0 \times 10^{17} \text{ cm}^{-2}$ , the profile of implants continuously shifts toward the surface. Such a profile shift results from the fact that most of the Cu atoms have been sputtered and the remaining atoms are mainly Zn atoms because the atomic mass of Zn is slightly larger than that of Cu atoms.

In the case of noble-metal NPs embedded into dielectrics, the distinctive SPR absorption, triggered by the complex interplay between the modified free electrons and interband absorptions, is an important fingerprint of NPs formation.<sup>12</sup> Therefore, the optical absorption properties of the prepared samples were first measured, and the corresponding results are given in Figure 3. The Cu sample presents a clear absorption band around 570 nm, which can be assigned to the SPR of Cu NPs.<sup>7</sup> After post implantation of Zn ions at a fluence of  $1.0 \times 10^{16} \text{ cm}^{-2}$ , the Cu SPR absorption is remarkably enhanced accompanied with a blue shift of 9 nm, which could be attributed to the increase of the partial dielectric constant around Cu NPs and to the introduction of Zn into Cu NPs owing to post Zn ion implantation.<sup>27</sup> For the highest Zn ion fluence used (i.e.,  $1.0 \times 10^{17} \text{ cm}^{-2}$ ), it was found that a strong absorption band appears around 250 nm, which is quite different from that detected in the Cu sample. Such a band has been widely detected in high-fluence Zn-implanted  $\text{SiO}_2$  substrate and is generally ascribed to the formation of Zn NPs into  $\text{SiO}_2$ .<sup>28,29</sup> Actually, as seen from Figure 1d, after post Zn ion implantation at high fluence, most of the Cu atoms have

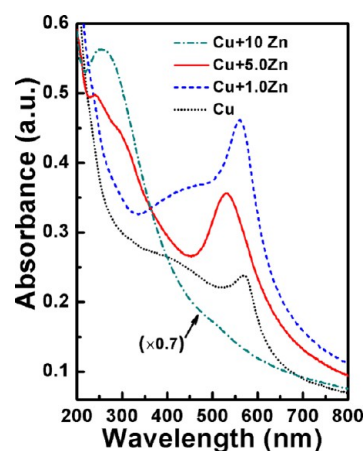


**Figure 3.** Optical absorption spectra of the Cu, Cu + 1.0 Zn, Cu + 5.0 Zn, and Cu + 10 Zn samples.

been sputtered and Zn with a high concentration remains in the subsurface region, which results in the formation of Zn NPs. Interestingly, for the post Zn ions implanted at the intermediate fluence (i.e.,  $5.0 \times 10^{16} \text{ cm}^{-2}$ ), the absorption spectrum presents a strong absorption peak at 530 nm together with a wide absorption band in the range of 240–295 nm. The wide absorption band could be related to the  $B_2$  absorption band ( $\sim 240 \text{ nm}$ ) of the pure  $\alpha\text{-SiO}_2$ <sup>30</sup> as well as the formation of small Zn and/or Zn-rich NPs in a deep region where a large quantity of Zn atoms are presented, as shown in Figure 1c. However, the absorption peak at 530 nm most probably comes from a superposition of SPR peaks of Cu–Zn alloy and residual Cu NPs because most Cu and Zn overlap in depth profiles and the high concentration of Cu presents near the sample surface (Figure 1c). The formation of CuZn alloy NPs in such a case will be further confirmed by GIXRD and XTEM measurements.

Figure 4 shows the GIXRD patterns recorded in the Cu, Cu + 1.0 Zn, Cu + 5.0 Zn, and Cu + 10 Zn samples. For

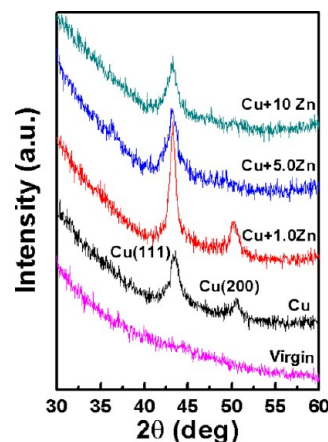


**Figure 4.** GIXRD patterns of the virgin silica, Cu, Cu + 1.0 Zn, Cu + 5.0 Zn, and Cu + 10 Zn samples.

comparison, the GIXRD pattern from the virgin silica (i.e., silica without implantation) is also given. From the figure, it is clear that the baselines of all of the implanted samples are similar to that of the virgin silica substrate, suggesting that the baseline is from the substrate but not from the effects of NPs formed by ion implantation. In the GIXRD pattern of the Cu sample, two



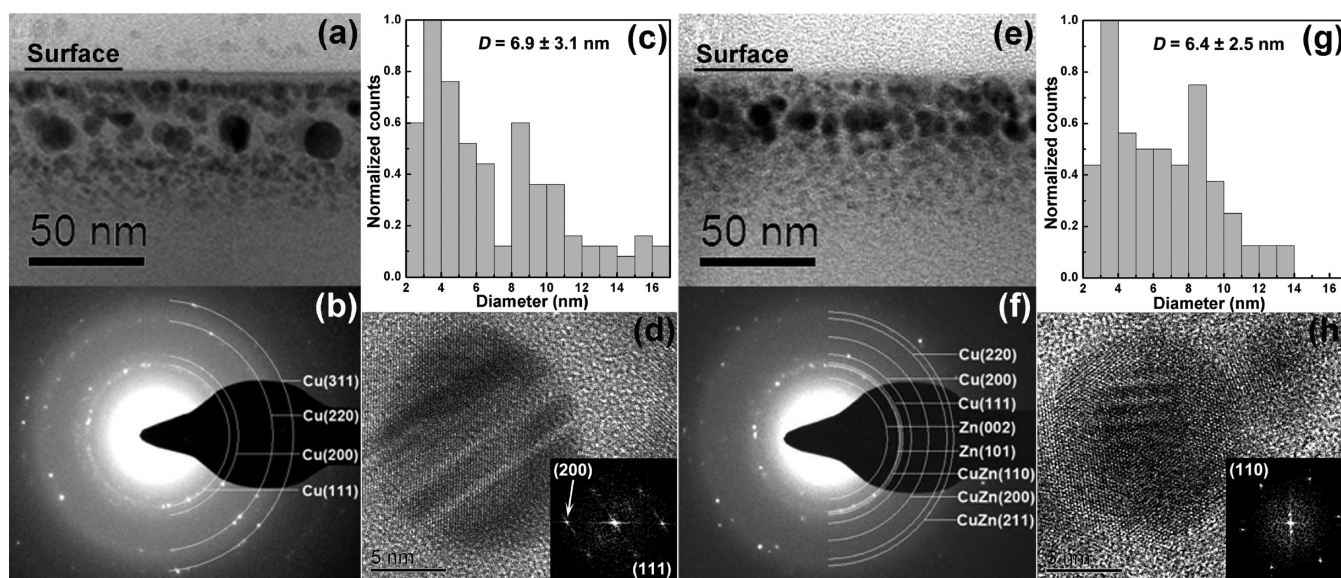


**Figure 5.** XTEM results of the (a–d) Cu and (e–h) Cu + 5.0 Zn samples. (a, e) Overall morphologies and (b, f) corresponding SAED patterns for each image. (c, g) Particle size distributions. Corresponding average diameters,  $D$ , are calculated for each case. (d, h) Typical HRTEM micrographs together with the corresponding FFT patterns.

diffraction peaks at  $43.4^\circ$  and  $50.4^\circ$  are revealed, which can be assigned to Cu (111) and Cu (200), respectively. The result confirms the formation of Cu NPs. After Zn ion implantation at the fluence of  $1.0 \times 10^{16} \text{ cm}^{-2}$ , although similar diffraction peaks are found, both of their intensities are significantly enhanced with a slight peak shift to low diffraction angles. Similar diffraction patterns indicate that the formed NPs are still Cu NPs. The slight shifts of peak positions toward low angles directly results from the lattice expand induced by the incorporation of Zn atoms into the Cu lattices.<sup>31,32</sup> The increased peak intensity could be attributed to the following factors. First, owing to Zn ion-beam heating, lattice defects generated in the Cu NPs would be partially recovered. This point is supported by the shoulder around 430 nm in the absorption spectrum of the Cu + 1.0 Zn sample (Figure 3) because the transformation from amorphous Cu NPs to crystalline ones can indeed lead to the increase of optical absorption at short wavelengths.<sup>33</sup> Second, ion-beam heating also results in the slight increases of the average size and volume fraction of Cu NPs.<sup>27</sup> Finally, because the (111) orientation has the minimum surface energy in face-centered cubic (fcc) crystals, the sharp and strong Cu (111) peak could also relate to the preferred grain growth along the (111) orientation.<sup>34,35</sup>

As for post Zn ion implantation at the fluence of  $1.0 \times 10^{17} \text{ cm}^{-2}$  (i.e., the Cu + 10 Zn sample), only a symmetric diffraction peak appears at about  $43.2^\circ$ . This diffraction angle is very similar to that of the Zn (101) plane, which means that the formed particles are mainly Zn NPs, as discussed for Figure 3. The GIXRD spectrum of the Cu + 5.0 Zn sample also exhibits a diffraction signal at  $43.2^\circ$ . The same peak position with that of the Zn (101) plane makes it difficult to identify directly the formation of Cu–Zn alloy NPs. Nevertheless, its asymmetry and higher intensity compared with those from the Cu and Cu + 10 Zn samples in combination with the optical absorption spectrum of the Cu + 5.0 Zn sample suggest that this diffraction peak most probably stems from an overlap of the diffraction peaks from metal Cu, Zn, and Cu–Zn alloy NPs.

To characterize further the structures and size distributions of the formed NPs, XTEM measurements were performed for the Cu and Cu + 5.0 Zn samples. The typical results are shown in Figure 5. The Cu ion implantation results in the formation of spherical NPs, which are distributed in a depth range of 4–55 nm, as shown in Figure 5a. The formed NPs exhibit a wide size distribution from 2 to 17 nm with a mean size of  $6.9 \pm 3.1 \text{ nm}$  (Figure 5c). Moreover, it is clear that NPs with large sizes are mainly located in the middle layer, whereas those with small sizes are distributed at both sides of the layer. Besides, results from the SAED pattern (Figure 5b) and fast Fourier transform (FFT) pattern for one of the NPs (insert in Figure 5d) confirm that the formed NPs are fcc Cu. In addition, many defects could also be observed in the formed NPs. As an example, Figure 5d presents a high-resolution TEM (HRTEM) image of one NP with lattice partial distortion.

As for the Cu + 5.0 Zn sample, XTEM observations show that the thickness of the layer containing NPs is similar to that of the Cu sample, as given in Figure 5e. However, large NPs are mainly distributed in a narrow region close to the sample surface, whereas small ones predominate in the deep region and present a broad distribution. Formation of the large NPs near the surface can be related to the sputtering-induced shift of the concentration profile of Cu atoms toward the sample surface. As a result, the Cu concentration near the surface becomes high and therefore the large NPs can be formed. Owing to the shift of the Cu concentration profile toward the surface side and the similar projected ranges of Zn and Cu ions, the small NPs in the deep region are probably Zn and/or Zn-rich alloy. Again, noting the ion-beam heating,<sup>36</sup> cascade collisions process,<sup>37</sup> and the high diffusivity of Zn atoms in  $\text{SiO}_2$ ,<sup>23</sup> small NPs with a broad distribution can be expected. In addition, according to Figure 5e,g, NPs formed in the Cu + 5.0 Zn sample also exhibit several interesting features compared with those in the Cu sample, such as a higher volume fraction, smaller size, and narrower size distribution. All of these are very conducive to enhancing the effective third-order optical susceptibility.<sup>1,38</sup> The result from the SAED pattern demonstrates that there exists three diffraction rings, matching well with the CuZn

(110), (200), and (211) planes, respectively, as shown in Figure 5f. This finding clearly indicates that body-centered cubic (bcc) CuZn alloy NPs were synthesized in the Cu + 5.0 Zn sample. According to the overlap region of the Cu and Zn atoms as shown in Figure 1c, one can argue that the formation of CuZn alloy NPs could be predominated in the shallow region beneath the surface where large NPs are mainly distributed. To verify this speculation, HRTEM observation was carried out for one of the large NPs. The obtained image together with its corresponding FFT pattern is presented in Figure 5h. One can see that the FFT pattern shows a 6-fold symmetry and lattice spacings consistent with bcc structures,<sup>39</sup> suggesting that the particle could be a CuZn alloy NP rather than a fcc Cu or hexagonal-close-packed (hcp) Zn NP. Finally, it should be pointed out that the SAED pattern in Figure 5f also exhibits the diffraction spots of Cu and Zn NPs. The Cu diffraction signal could originate from the survival of the large Cu NPs in the shallow region, as shown in Figure 5a, whereas the Zn diffraction signal supports the existence of Zn NPs in the deep region. Thus, a mixture of Cu, CuZn, and Zn NPs in the Cu + 5.0 Zn sample can be expected, and its absorption spectrum displays a very complicated absorption behavior, as previously given in Figure 3.

The high-angle angular dark-field (HAADF) image for the Cu + 5.0 Zn sample is shown in Figure S1a in the Supporting Information. Figure S1b in the Supporting Information shows line-scanned average atomic-number profiles of Cu and Zn crossing the whole implanted layer. It was found that the signal of Cu is much stronger than that of Zn near the sample surface. In the depth range of about 7–28 nm, the concentrations of Cu and Zn are comparable. In particular, the intensity profiles (see the inset in Figure S1b) recorded for one NP in this region exhibit nearly equal proportions of Cu and Zn, indicating that the NP could be a CuZn alloy particle. In the deeper region, the amount of Zn atoms becomes higher than that of Cu atoms. Thus, small Zn and/or Zn-rich alloy NPs could exist in such a region. The above depth profiles of Cu and Zn are very close to those shown in Figure 1c and further support the formation of CuZn alloy as well as the survival of Cu and Zn NPs.

To detect the thermal stability of the formed CuZn alloy NPs, the Cu + 5.0 Zn sample was further furnace-annealed in nitrogen ambient at elevated temperatures, and the corresponding absorption spectra were measured. The recorded optical absorption spectra are shown in Figure 6. From the figure, one can see that subsequent annealing of the Cu + 5.0 Zn sample induces a series of interesting changes in the optical absorption behaviors, which show strong dependence on the applied temperature. First, for the wide absorption band in the wavelength range of 240–295 nm, its intensity gradually decreases with increasing the annealing temperature and disappears at 450 °C and higher. Such variation could be associated with the thermal growth of Zn NPs at low temperature and diffusion of Zn atoms at high temperature. During low-temperature annealing, Zn NPs undergoes thermal growth by absorbing the smaller Zn NPs and the isolated Zn atoms (i.e., the Ostwald ripening process).<sup>40</sup> Consequently, the concentration of Zn NPs decreases. However, when the temperature increases to 450 °C, which is higher than the melting point of bulk Zn (about 419.5 °C), all Zn NPs could melt, accompanied by the diffusion of Zn atoms toward the shallow region that has the lower potential-energy sites.<sup>41</sup> Therefore, the Zn-related absorption band would disappear.

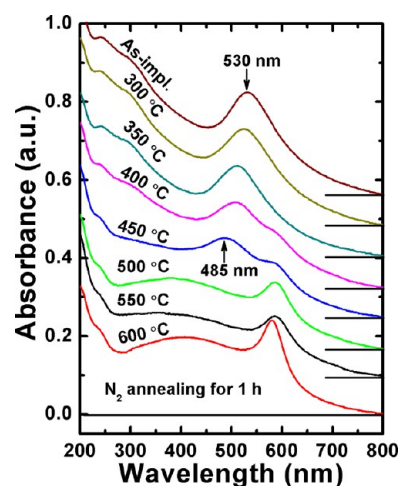


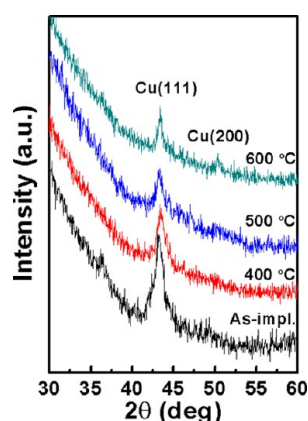
**Figure 6.** Optical absorption spectra of the Cu + 5.0 Zn sample before and after annealing at different temperatures. The spectra are vertically shifted from each other for clarity, with horizontal lines showing the zero level of each spectrum.

Concerning the absorption band around 530 nm, subsequent annealing at temperatures up to 350 °C leads to a shift of the band toward the low-wavelength range without a significant change in its intensity. The blue shift of the band could be related to the thermally driven diffusion of Zn atoms. As mentioned above, smaller Zn NPs could be melted during annealing because of their low melting point, and release of Zn atoms would occur. Owing to the fact that Zn atoms have a relatively high diffusivity in SiO<sub>2</sub><sup>23</sup> and that Cu and Zn have high miscibility as well as negative mixing heat and interdiffusion coefficients,<sup>20–22</sup> the isolated Zn atoms together with those released from the smaller Zn NPs could diffuse into the shallow region where CuZn alloy NPs are present and participate in the nucleation and growth of these NPs. Therefore, CuZn alloy NPs with more Zn content could be formed. Actually, Cokoja et al.<sup>42</sup> illustrated that the SPR absorption peak of a nanocolloidal Cu–Zn alloy could be shifted to low wavelengths by appropriately increasing the content of the Zn composition. For annealing temperatures in the range of 400–450 °C, it is clear that besides the blue shift of the main absorption peak related to CuZn alloy NPs, a shoulder absorption band appears at a wavelength around 585 nm. Decomposition of the absorption band into two peaks indicates that structures of the CuZn NPs have been largely modified during annealing in this temperature range. On the basis of the observed optical absorption variation, we propose that in such a temperature range, the most probable structure of the formed NPs is a core–shell one (i.e., a Cu predominated core with a Zn-rich alloy shell). The reasons for this are as follows. As is known, thermal treatment could lead to decomposition of CuZn alloy NPs and diffusion of the involved atoms. Noting that Zn atoms have higher diffusivity than that of Cu atoms,<sup>23,43</sup> the segregation of Zn toward the alloy NPs surface occurs according to the Kirkendall effect,<sup>43–45</sup> resulting in the formation of NPs with Cu-predominated cores and Zn-rich alloy shells. The Cu-predominated cores result in an absorption band around 585 nm, whereas the Zn-rich alloy shells give rise to the absorption band in the low-wavelength range. In fact, the occurrence of two SPR absorption peaks has been well-demonstrated in an Au–Au<sub>x</sub>Ag<sub>1–x</sub> core–shell system.<sup>46</sup> Furthermore, isolated Zn atoms in the substrate



could be absorbed by alloy shells via an Ostwald ripening process,<sup>40</sup> resulting in a further increase of the Zn content there. Consequently, the SPR absorption of CuZn continuously shifts to the low wavelength, as demonstrated in Figure 6. At 500 °C, the alloy NP-related SPR peak disappears, and the absorption peak attributed to the Cu NPs is pronounced. This result demonstrates that decomposition of CuZn alloy NPs via Zn diffusion from the alloys is completed at 500 °C. Therefore, Cu NPs are left behind at the original sites and cause a SPR absorption peak at about 585 nm. In addition, it should be pointed out that the outward-diffusion Zn atoms could aggregate around the Cu NPs, resulting in the formation of Zn or Zn-related compound shells. The formation of NPs with core-shell structures was actually detected in the 500 °C annealed Cu + 5.0 Zn sample, which will be presented later. Further increasing the annealing temperature to 550 °C only leads to a slight change in the Cu SPR absorption peak. However, after 600 °C annealing, the Cu SPR peak increases and blue shifts to 580 nm from 585 nm as compared with that in the 500 °C annealed sample. The changes can be attributed to the synergy of the aggregation and growth of Cu NPs driven by thermal treatment<sup>47</sup> and the partial recovery of dielectric constant around Cu NPs because of the diffusion of Zn atoms toward the substrate surface.<sup>23</sup>

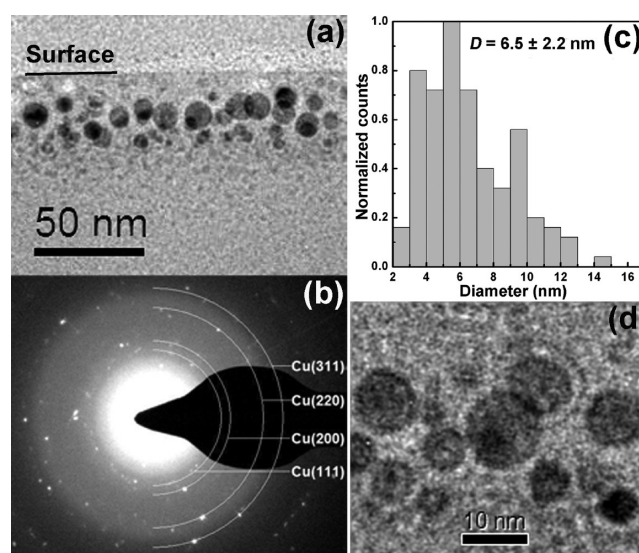
The decomposition of CuZn alloy NPs under annealing at elevated temperatures has been further demonstrated by GIXRD measurements, as shown in Figure 7. From Figure 7,



**Figure 7.** GIXRD patterns of the Cu + 5.0 Zn sample before and after annealing at elevated temperatures.

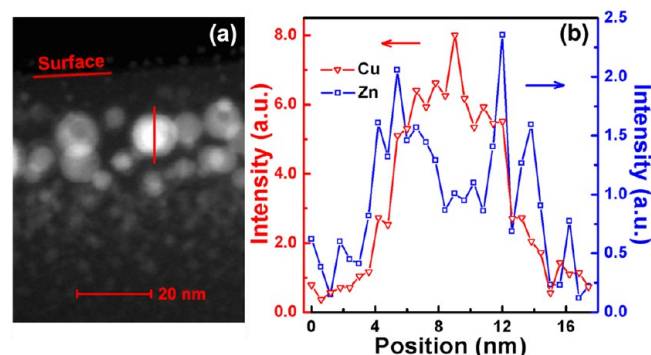
it can be seen that after annealing at temperatures of 500 °C and higher both diffraction peaks ascribed to Cu (111) and Cu (200) appear, demonstrating that decomposition of CuZn alloy NPs has been completed and the predominated NPs are Cu.

Figure 8 shows the XTEM micrograph together with particle size distribution of the Cu + 5.0 Zn sample annealed at 500 °C. By comparing Figure 5, panels e and g, we can see that 500 °C annealing causes only modest changes in the spatial and size distributions of large NPs. However, owing to the low melting point of Zn NPs and the fast diffusion of Zn atoms, the small Zn-related nanoclusters situated at end of the implanted layer sharply reduces, and the corresponding layer involving NPs becomes narrow. The SAED pattern confirms that the finally formed NPs are mainly fcc Cu NPs (Figure 8b), supporting the conclusions from the optical absorption and GIXRD spectra. Moreover, with a close view of the NPs, one can see that most of the NPs present distinct core-shell structures, as shown in



**Figure 8.** TEM results of the Cu + 5.0 Zn sample after 500 °C annealing. (a) Overall morphology, (b) corresponding SAED pattern, (c) particle size distribution and calculated average diameter,  $D$ , and (d) close view of the formed NPs.

Figure 8d. By performing EDXS measurements on a single particle (Figure 9), it is clear that the Cu atoms are mainly



**Figure 9.** (a) HAADF image of the Cu + 5.0 Zn sample after 500 °C annealing. (b) Average atomic-number profiles of Cu and Zn across one of the large particles in panel a. The symbols are the experimental data, and the lines are drawn as a guide to the eye.

contributing to the core of the NP, whereas the shell of NP could be made up of Zn or Zn-related compounds. The results indicate that during diffusion of Zn from decomposed CuZn alloy NPs some Zn atoms could be aggregated around the Cu cores, resulting in the formation of a thin shell structure.

Finally, to emphasize the possible processes occurring in the CuZn alloys NPs formed in the Cu + 5.0 Zn sample during subsequent annealing, the schematically depicted processes for one typical CuZn alloy NP is presented in Figure 10 on the basis of the experimental findings. In the low temperature range of 300–350 °C (Figure 10b), thermal annealing could induce decomposition of Zn nanostructures that are distributed around the alloy NPs, and the release of Zn atoms could be expected. Owing to the high diffusivity of Zn in SiO<sub>2</sub>, thermally driven diffusion of these Zn atoms toward CuZn alloy NPs occurs, which gives rise to the increased Zn content in the NPs. As a result, the SPR absorption band exhibits a blue shift. The process could be referred to as a realloying of the NPs. In the

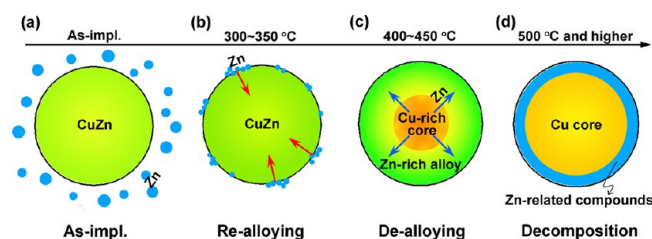


**Figure 10.** Schematic diagram showing the annealing-induced possible processes in one CuZn alloy NP formed in the Cu + 5.0 Zn sample and the final structure: (a) one CuZn alloy NP, (b) Zn diffusion-driven realloying process, (c) Zn diffusion-driven formation of the Cu-rich core and Zn-rich alloy shell structure, and (d) final NP structure with a Cu core and Zn-related compound shell.

intermediate temperature range of 400–450 °C, nearly all of the Zn NPs are decomposed because of the low melting point, as mentioned earlier. The thermally driven realloying of CuZn would finish. However, decomposition of CuZn alloy NPs will take place. Owing to the fact that Zn has much higher diffusivity than that of Cu, the thermal diffusion of Zn should predominate. According to our results, the decomposition of CuZn alloy NPs most probably appears in the central regions of NPs rather than in the peripheral regions of the NPs. Accompanying the decomposition of the CuZn alloy NPs is the segregation of Zn toward the alloy NP surface (i.e., Kirkendall effect), resulting in the formation of Zn-rich alloy shells surrounding Cu-rich cores, as schematically presented in Figure 10c. Such core-shell structures give rise to two distinguished SPR absorption bands that are mutually superimposed, as is clearly demonstrated in Figure 6. The above-mentioned process could be referred to as a dealloying of the NPs. Increasing the temperature causes further decomposition of the CuZn alloy. Therefore, the thickness of the CuZn alloy shell gradually reduces. As annealing temperatures reach 500 °C and higher, the decomposition of the CuZn alloy NPs finishes. Besides the diffusion of Zn toward both the substrate surface and bulk, some of the Zn atoms could remain in the vicinity of the NPs and chemically react with substrate elements, forming more stable Zn-related compounds, such as ZnO, Zn<sub>2</sub>SiO<sub>4</sub>, and others.<sup>48–50</sup> Thus, Cu NPs surrounded by thin Zn-related compound shells could be created, as illustrated in Figure 10d.

#### 4. CONCLUSIONS

The effects of post Zn implantation on the structures and optical absorption properties of Cu NPs embedded into SiO<sub>2</sub> were investigated in detail. At a low fluence of  $1.0 \times 10^{16} \text{ cm}^{-2}$ , post Zn ion implantation significantly enhanced Cu SPR absorption by modifying the partial dielectric environment around the Cu NPs. At a high fluence of  $1.0 \times 10^{17} \text{ cm}^{-2}$ , owing to heavy sputtering effects from the post Zn implantation, the presynthesized Cu NPs are nearly removed and consequently the formed colloids are mainly attributed to Zn NPs. However, as Zn ions were implanted at an intermediate fluence of  $5.0 \times 10^{16} \text{ cm}^{-2}$ , bcc CuZn alloy NPs can be formed even in the as-implanted state, which gives a pronounced SPR absorption band situated between those for the Cu and Zn NPs. During subsequent annealing, the formed CuZn alloy NPs undertakes two distinguished processes (i.e., realloying and dealloying) owing to thermally driven Zn diffusion and its dependence on temperature, which causes the corresponding optical absorption to change over a wide range. Moreover, owing to the outward

diffusion of Zn atoms from alloy NPs during alloy decomposition processes, nanostructures with Cu-rich cores and Zn-related compound shells were formed. These findings provide an effective route to modulate both the structures and optical absorption properties of Cu NPs embedded in dielectrics, which could be of interest for the fabrication of SPR-based optical sensors, waveguides, antibacterial materials, and others.

#### ■ ASSOCIATED CONTENT

##### Supporting Information

EDXS and X-ray photoelectron spectroscopy (XPS) measurements. This material is available free of charge via the Internet at <http://pubs.acs.org>.

#### ■ AUTHOR INFORMATION

##### Corresponding Author

\*E-mail: [liuchanglong@tju.edu.cn](mailto:liuchanglong@tju.edu.cn).

##### Notes

The authors declare no competing financial interest.

#### ■ ACKNOWLEDGMENTS

We acknowledge financial support from the Natural Science Foundation of China (NSFC) (nos. 11175129 and 11175235) and the Natural Science Foundation of Tianjin (no. 12JCZDJC 26900). We are also grateful to Dr. Wenbo Mi for helpful discussions and Dr. Haitao Dai for helping with the UV–vis optical absorption measurements.

#### ■ REFERENCES

- (1) Meldrum, A.; Haglund, R. F., Jr; Boatner, L. A.; White, C. W. *Adv. Mater.* **2001**, *13*, 1431–1444.
- (2) Inouye, H.; Tanaka, K.; Tanahashi, I.; Hattori, T.; Nakatsuka, H. *Jpn. J. Appl. Phys., Part 1* **2000**, *39*, 5132–5133.
- (3) Dong, P. P.; Lin, Y. Y.; Deng, J. J.; Di, J. W. *ACS Appl. Mater. Interfaces* **2013**, *5*, 2392–2399.
- (4) Sharma, A. K.; Jha, R.; Gupta, B. D. *IEEE Sens. J.* **2007**, *7*, 1118–1129.
- (5) Fuertes, G.; Sánchez-Muñoz, O. L.; Pedrueza, E.; Abderrafi, K.; Salgado, J.; Jiménez, E. *Langmuir* **2011**, *27*, 2826–2833.
- (6) Ferrando, R.; Jellinek, J.; Johnston, R. L. *Chem. Rev.* **2008**, *108*, 845–910.
- (7) Mattei, G.; Mazzoldi, P.; Bernas, H. *Top. Appl. Phys.* **2010**, *116*, 287–316.
- (8) Catarino, N.; Nogales, E.; Franco, N.; Darakchieva, V.; Miranda, S. M. C.; Méndez, B.; Alves, E.; Marques, J. G.; Lorenz, K. *EPL* **2012**, *97*, 68004.
- (9) Cesca, T.; Calvelli, P.; Battaglin, G.; Mazzoldi, P.; Mattei, G. *Opt. Express* **2012**, *20*, 4537–4547.
- (10) Haug, J.; Kruth, H.; Dubiel, M.; Hofmeister, H.; Haas, S.; Tatchev, D.; Hoell, A. *Nanotechnology* **2009**, *20*, 505705.
- (11) Cattaruzza, E.; Battaglin, G.; Gonella, F.; Polloni, R.; Scremin, B. F.; Mattei, G.; Mazzoldi, P.; Sada, C. *Appl. Surf. Sci.* **2007**, *254*, 1017–1021.
- (12) Mattei, G. *Nucl. Instrum. Methods Phys. Res., Sect. B* **2002**, *191*, 323–332.
- (13) Jain, I. P.; Agarwal, G. *Surf. Sci. Rep.* **2011**, *66*, 77–172.
- (14) Swann, C. P. *Nucl. Instrum. Methods Phys. Res., Sect. B* **1995**, *104*, 576–583.
- (15) Pithawalla, Y. B.; El-Shall, M. S.; Deevi, S. *Scr. Mater.* **2003**, *48*, 671–676.
- (16) Tang, Q. G.; Meng, J. P.; Liang, J. S.; Nie, L.; Li, Y. X. *J. Alloys Compd.* **2010**, *491*, 242–247.
- (17) Wang, G. G.; Zhu, L. Q.; Liu, H. C.; Li, W. P. *Mater. Lett.* **2011**, *65*, 3095–3097.



- (18) Wang, Z. W.; Zhu, L. Q.; Li, W. P.; Liu, H. C. *ACS Appl. Mater. Interfaces* **2013**, *5*, 4808–4814.
- (19) Xi, J. Y.; Wang, Z. F.; Lu, G. X. *Appl. Catal., A* **2002**, *225*, 77–86.
- (20) Hume-Rothery, W.; Mabbott, G. W.; Channel Evans, K. M. *Philos. Trans. R. Soc., A* **1934**, *233*, 1–97.
- (21) Yazawa, A.; Gubčová, A. *Mater. Trans. JIM* **1970**, *11*, 419–423.
- (22) Pickering, H. W.; Wagner, C. J. *Electrochem. Soc.* **1967**, *114*, 698–706.
- (23) Wang, J.; Zhang, L. H.; Zhang, X. D.; Shen, Y. Y.; Liu, C. L. *J. Alloys Compd.* **2013**, *549*, 231–237.
- (24) Amekura, H.; Ohnuma, M.; Kishimoto, N.; Buchal, Ch.; Mantl, S. *J. Appl. Phys.* **2008**, *104*, 114309-1–114309-8.
- (25) Gnaser, H.; Brodyanski, A.; Reuscher, B. *Surf. Interface Anal.* **2008**, *40*, 1415–1422.
- (26) Ziegler, J. F.; Ziegler, M. D.; Biersack, J. P. *Nucl. Instrum. Methods Phys. Res., Sect. B* **2010**, *268*, 1818–1823.
- (27) Jia, G. Y.; Wang, J.; Zhang, L. H.; Liu, H. X.; Xu, R.; Liu, C. L. *EPL* **2013**, *101*, 57005.
- (28) Shen, Y. Y.; Li, X.; Wang, Z.; Zhang, L. L.; Zhang, D. C.; Li, M. K.; Yuan, B.; Li, Z. D.; Liu, C. L. *J. Cryst. Growth* **2009**, *311*, 4605–4609.
- (29) Amekura, H.; Umeda, N.; Sakuma, Y.; Kishimoto, N.; Buchal, Ch. *Appl. Phys. Lett.* **2005**, *87*, 013109-1–013109-3.
- (30) Marshall, C. D.; Speth, J. A.; Payne, S. A. *J. Non-Cryst. Solids* **1997**, *212*, 59–73.
- (31) Omar, S.; Wachsman, E. D.; Nino, J. C. *Solid State Ionics* **2008**, *178*, 1890–1897.
- (32) Wu, J. B.; Li, P. P.; Pan, Y.; Warren, S.; Yin, X.; Yang, H. *Chem. Soc. Rev.* **2012**, *41*, 8066–8074.
- (33) Amekura, H.; Johannessen, B.; Sprouster, D. J.; Ridgway, M. C. *Appl. Phys. Lett.* **2011**, *99*, 043102-1–043102-3.
- (34) Sikder, A. K.; Kumar, A.; Shukla, P.; Zantye, P. B.; Sanganaria, M. *J. Electron. Mater.* **2003**, *32*, 1028–1033.
- (35) Shinada, E.; Nagoshi, T.; Chang, T.-F. M.; Sone, M. *Mater. Sci. Semicond. Process.* **2013**, *16*, 633–639.
- (36) Volkert, C. A.; Minor, A. M. *MRS Bull.* **2007**, *32*, 389–399.
- (37) Ren, F.; Jiang, C. Z.; Liu, C.; Wang, J. B. *Appl. Phys. Lett.* **2006**, *88*, 183114-1–183114-3.
- (38) Stepanov, A. L. *Rev. Adv. Mater. Sci.* **2011**, *27*, 115–145.
- (39) Geng, H.; Heckman, J. W.; Pratt, W. P.; Bass, J.; Espinosa, F. J.; Conradson, S. D.; Lederman, D.; Crimp, M. A. *J. Appl. Phys.* **1999**, *86*, 4166–4175.
- (40) Voorhees, P. W. *J. Stat. Phys.* **1985**, *38*, 231–252.
- (41) Xiao, X. H.; Ren, F.; Wang, J. B.; Liu, C.; Jiang, C. Z. *Mater. Lett.* **2007**, *61*, 4435–4437.
- (42) Cokoja, M.; Parala, H.; Schröter, M. K.; Birkner, A.; van den Berg, M. W. E.; Klementiev, K. V.; Grünert, W.; Fischer, R. A. *J. Mater. Chem.* **2006**, *16*, 2420–2428.
- (43) Fan, H. J.; Gösele, U.; Zacharias, M. *Small* **2007**, *3*, 1660–1671.
- (44) Xu, Y.-H.; Wang, J.-P. *Adv. Mater.* **2008**, *20*, 994–999.
- (45) Heggen, M.; Oezaslan, M.; Houben, L.; Strasser, P. *J. Phys. Chem. C* **2012**, *116*, 19073–19083.
- (46) Wu, W.; Njoki, P. N.; Han, H.; Zhao, H.; Schiff, E. A.; Lutz, P. S.; Solomon, L.; Matthews, S.; Maye, M. M. *J. Phys. Chem. C* **2011**, *115*, 9933–9942.
- (47) Stepanov, A. L.; Khaibullin, I. B. *Rev. Adv. Mater. Sci.* **2005**, *9*, 109–129.
- (48) Cattaruzza, E. *Nucl. Instrum. Methods Phys. Res., Sect. B* **2000**, *169*, 141–155.
- (49) Amekura, H.; Yoshitake, M.; Plaksin, O. A.; Kishimoto, N.; Buchal, Ch.; Mantl, S. *Appl. Phys. Lett.* **2007**, *91*, 063113-1–063113-3.
- (50) Wang, J.; Jia, G. Y.; Zhang, B.; Liu, H. X.; Liu, C. L. *J. Appl. Phys.* **2013**, *113*, 034304-1–034304-8.